Ablation of submicrometer holes using an extreme-ultraviolet laser

Andrew K. Rossall,[1, a] Ilya Kuznetsov,[2] Valentin Aslanyan,[1] Greg J. Tallents,[1] Jorge J. Rocca,[2] and Carmen S. Menoni[2]

[1] *York Plasma Institute, University of York, Heslington, York, YO10 5DD, UK*

[2] *Centre for Extreme Ultraviolet Science and Technology and Department of Electrical and Computer Engineering, Colorado State University, Fort Collins, Colorado 80523*

(Dated: May 11, 2015)

Simulations and experiments are used to study extreme ultraviolet laser drilling of sub-micrometer holes. The ablation process has been studied with a 2D Eulerian hydrodynamic code that includes bound-free absorption processes relevant to the interaction of EUV lasers with a solid material. Good agreement is observed between the simulated and measured ablated depths for on target irradiances of up to 1×10^{10} W cm^{-2}. An increase in the irradiance to 1×10^{12} W cm^{-2} is predicted to ablate material to a depth of 3.8 μm from a single pulse with a hole diameter 3 to 4 times larger than the focal spot size. The model allows for the simulation of the interaction of a laser pulse with the crater created by a previous shot. Multiple pulse, lower fluence irradiation configurations under optimized focusing conditions, i.e. approaching the diffraction limit, are shown to be advantageous for applications requiring mesoscale (100nm-1μm) features and a high level of control over the ablation profile.

PACS numbers: 42.55.Vc, 32.80.Fb, 79.20.Eb, 52.65.Ww

[a] Email: andrew.rossall@york.ac.uk

I. INTRODUCTION

Considerable advances have been made in high fluence extreme ultra-violet (EUV) and X-ray laser technology as is shown by laser plasma based EUV lasers[1], free-electron lasers[2] and capillary discharge lasers[3–6]. With higher fluences and repetition rates up to 100Hz[7] now available, EUV and X-ray lasers can be used to directly generate strongly coupled plasmas. Targets irradiated by EUV lasers are heated predominantly via direct photo-ionization, as opposed to inverse bremsstrahlung as with traditional optical, infra-red (IR) and ultraviolet (UV) lasers. This results in typically lower plasma temperatures and higher particle densities[8]. With traditional laser produced plasmas, an expanding plume of plasma only allows absorption away from the target surface where the electron density has dropped below a critical value ($\simeq {}^{10^{21}}/_{\lambda_\mu^2}$ cm^{-3}, where λ_μ is the laser wavelength in units of microns). By reducing the wavelength into the EUV/X-ray region, the critical electron density is typically greater than solid and the laser photon energy, E_p, becomes sufficient to directly photo-ionise elemental components (ionisation energy E_i), transferring energy ($E_p - E_i$) to the ejected electron. As the critical electron density (the point at which the real part of the dielectric function goes to zero) is typically higher than solid, the laser is able to penetrate the expanding plasma plume and continue to heat the solid material directly throughout the duraction of the laser pulse. This differs from the interaction of optical, IR and UV pulses with solids where the majority of the pulse energy is absorbed within the expanding plasma plume via inverse bremsstrahlung. Reducing the lasing wavelength to the EUV/soft X-ray region also allows for a tighter focus, due to a reduction in the diffraction limit. The tighter focus is a potentially desirable property for a number of applications, for example, mesoscale machining[9], mass spectrometry[10] and the coating of refractory material onto substrates.

In order to promote research and to accelerate the development of industrial applications, there is a significant motivation to produce compact and affordable EUV/X-ray laser sources for use in parallel with large scale free electron laser facilities such as the European free electron laser, FLASH[11]. One such example is a table-top size soft X-ray laser system[12,13] based upon capillary discharge excitation of an Ar gas which causes lasing at 46.9nm with a pulse energy up to 0.8mJ[3,6] and a pulse length of 1.2ns[4].

The work presented here utilises a novel combination of fluid code modelling with atomic physics to simulate EUV/soft X-ray interaction with a solid, the laser energy deposition within the target, thermal energy transport and the subsequent ablative flow away from the target. Using a 2D hydrodynamic code, POLLUX[14–16], originally written to simulate optical and infra-red laser interaction, and adding new absorption and atomic physics enables the simulation of the ablative properties of EUV and X-ray lasers. A comparison between simulation and experiment is shown for a capillary discharge laser, operating at 46.9nm, ablating a planar parylene-N target under vacuum. Simulation results are then presented for higher irradiance and multiple pulse interactions demonstrating the significant potential benefits of capillary discharge lasers for high aspect ratio hole drilling.

II. POLLUX

The 2D Eulerian hydrodynamic code POLLUX, originally written at the University of York, was developed to model moderate irradiance (10^9 - 10^{14} W cm^{-2}) optical and infra-red laser irradiation of a solid target. With optical lasers, a strongly ionized plasma is produced which absorbs the incident laser beam. The code solves the three first-order quasi-linear partial differential equations of hydrodynamic flow using the flux corrected transport model of Boris and Book[17] with an upwind algorithm[18] for the first term. Energy absorption within the target has been modified to include photoionization processes relevant to EUV and X-ray interactions. Energy is absorbed by the plasma electrons through inverse bremsstrahlung and direct photo-ionization and distributed via electron-ion collisions. The energy transfer rate between electrons and ions is calculated using the smaller value of the Spitzer electron collision frequency[19] or the electron-phonon collision frequency[20]. For calculation of the equation-of-state (EOS) variables, POLLUX utilizes in-line hydrodynamic EOS subroutines from the Chart-D[21] equation-of-state package developed at Sandia National Laboratories and includes two phase transitions.

To properly calculate bound-free absorption processes within the target material, a model of atomic structure is used to account for transitions from both the ground and excited states. To achieve this, whilst keeping the runtime reasonable for a fluid code, a superconfiguration model[22] has been employed to reduce the number of levels to be considered. Ionisation dependant superconfigurations are calculated for an individual element by using the Flexible Atomic Code (FAC)[23] to solve the radial wavefunction. This provides detailed atomic structure, which is then post-processed to form a reduced data set of ionisation stages, atomic energy levels and photoionization cross-sections. As the produced plasma is close to solid density, the ionization energy, E_i, can be significantly lowered due to the presence of the surrounding electrons and ions. This ionization potential depression can cause pressure ionization, thus reducing the absorption of the laser in that region. Ion potential depression is accounted for using a modified model originally developed by Stewart and Pyatt[24]. Ionic and excited state populations are determined by assuming local thermodynamic equilibrium (LTE) and using the Saha-Boltzmann relation. Although the initial plasma state is highly non-equilibrated, it has been shown that due to the high densities involved, the plasma ionization equilibrates on a time-scale of tens of femtoseconds[25]. The fluid code simulations shown here operate on a hydrodynamic time-scale of > 1ps, therefore the LTE assumption is valid. An analytical approximation of the Kramers-Kronig relationship is used to determine temperature dependant atomic scattering factors and thus the refractive index of the plasma, and has been reported previously[26]. This combination of atomic physics modelling of laser absorption, EUV ray-tracing within the plasma including a temperature dependant refractive index and the simulation of the subsequent ablative flow from the target is a unique capability for the application of mesoscale machining.

III. EXPERIMENTAL BENCHMARKING

The benchmark simulation results shown here are for an Ar-based capillary discharge laser irradiating a planar parylene-N target, with a photon energy of 26.4 eV ($\lambda = 46.9$nm), a FWHM pulse length of 1200ps, and fluence ranging between 2 and 8 J cm^{-2}. Experimental measurements of the ablated depth in Parylene-N were conducted using a capillary discharge laser system developed at Colorado State University (CSU)[5].

The capillary discharge laser was focused, under vaccum, using a Fresnel zone plate with a numerical aperture of 0.12, where the smallest possible diameter of the first null of the Airy disk is $\sim$240nm. The spatial profile of the laser in the simulations is described by approximating the central lobe of the Airy disk as a Gaussian function. The diffraction limited spot size in this case would be a FWHM diameter of $\sim$ 207nm. In the experiments, craters with a FWHM diameter ranging between 650 and 850nm were ablated.

By varying the fluence over the range tested via experimental measurement, a comparison can be made to ascertain the accuracy of the code in the simulation of EUV ablation. Figure

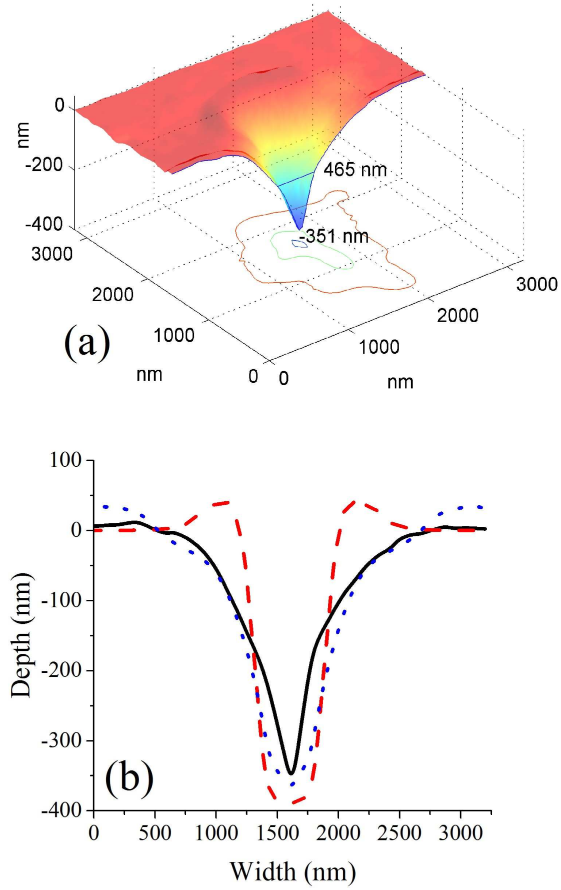

Figure 1. (Color online) (a) Experimentally obtained ablation profile. The FWHM and depth of the hole are indicated. The contours are cross sections of the ablated crater at 10, 50 and 90 percent of its depth. (b) Comparison with the simulated ablation profile, for a fluence of 7.7 J cm^{-2} (6×10^9 W cm^{-2}). The black solid line in (b) is a lineout of the experimental profile in (a). Simulated ablation profiles are shown for a laser with a Gaussian beam profile (red dashed) and a double Gaussian approximation of the central lobe (containing 92% of total energy) and side lobe (containing 8% of the total energy) of an Airy disk (blue dotted).

1(a) shows an image of an ablated parylene-N target measured using atomic force microscopy (AFM), after the shot, for the fluence of 7.7 J cm^{-2}. The corresponding line-out through the central ablated region is shown (figure 1(b)) with a comparison to two computed ablation profiles. The first using a Gaussian profile as described and the second using a double Gaussian profile to approximate an Airy pattern with 92% of the energy in the central lobe and 8% of the energy in a side lobe. Figure 2 shows a comparison between the ablated depth in Parylene-N measured experimentally and the ablated depth predicted through simulation.

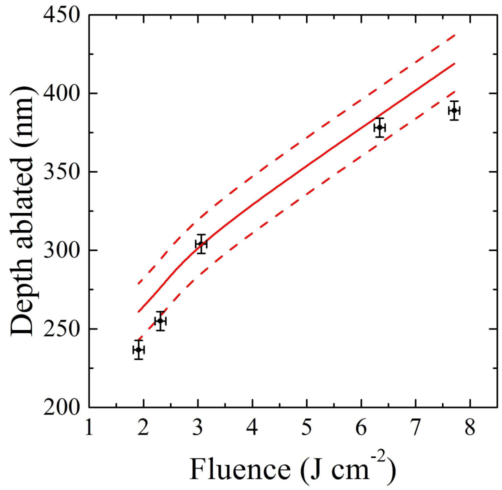

Figure 2. (Color online) Comparison between experimental ablated depth measurements (squares) and simulations (solid line) as a function of EUV laser fluence on target. The dashed lines indicate the resolution of the Eulerian mesh used in the simulations.

The depth of ablation in the simulation is taken after 1300ps (t = 600ps is the peak of the pulse) at the point at which the ion temperature drops below the melting point, which for Parylene-N is 0.06eV (420°C). The dashed lines indicate the resolution of the Eulerian mesh used in the simulations which is limited by the Courant-Friedrichs-Lewy condition[27].

Good agreement is observed between the ablated depth predicted via simulation and the experimentally observed ablated depth, giving confidence to the computational algorithms utilised. Current capillary discharge lasers are capable of pulse energies up to 0.8 mJ [6], hence irradiances approaching 1×10^{12} W cm^{-2} could be achievable with appropriate collection and focussing optics.

IV. SIMULATION RESULTS AND DISCUSSION

To explore the ablative capabilities of this technology, the effect of varying the irradiance from 1×10^9 W cm^{-2} to 1×10^{12} W cm^{-2} has been simulated, the results of which are shown in figure 3. Ablated depths of 3.8 μm per pulse are observed for the highest irradiance with a lateral hole size of 2.2μm (FWHM) for a 0.5μm diameter (FWHM) focal width. High aspect ratio, sub-micron size surface features are achievable, providing the system is optimised to inhibit lateral heat transport within the target. Figure 3 shows ablation profiles as a function of irradiance after 1300 ps of irradiation and demonstrates

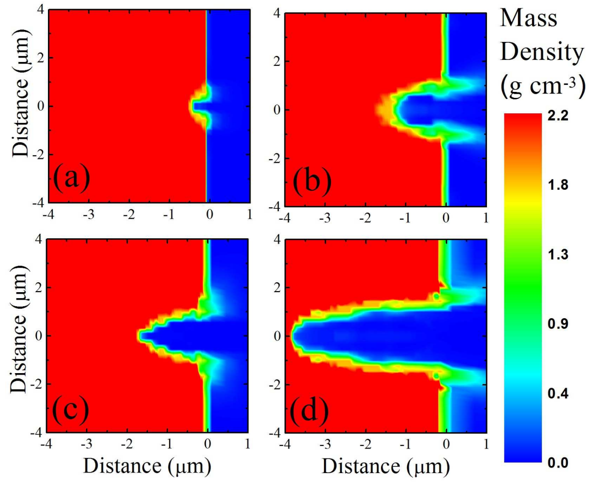

Figure 3. (Color online) Simulated ablation profiles at $t = 1300$ps for (a) 1×10^{9} W cm^{-2}, (b) 1×10^{10} W cm^{-2}, (c) 1×10^{11} W cm^{-2} and (d) 1×10^{12} W cm^{-2} with a focal spot diameter of 500nm.

that lateral heat transport increases the feature size with increasing fluence as one would expect due to the increase in localised energy deposition in the target. Typical predicted temperatures for the laser produced plasma range between 2 and 20eV with plasma flow velocities along the laser axis ranging between 10^{5} to 10^{7} cm s^{-1} , depending upon the laser irradiance. Further information regarding the plasma properties can be found in previously published work[16,26].

Ablation with a laser operating in the EUV wavelength range optimises energy deposition within the target. Parylene-N has $> 70\%$ transparency over the range of optical wavelengths, whereby photons at 46.9nm have a penetration depth of only 20nm in cold solid parylene-N. This leads to a highly localised deposition of energy in small volume, resulting in increased uniformity of heating and thus ablation. As the target material is heated, via bound-free absorption dominated by the carbon component of the material, ionization increases and the material becomes transparent as the 26.4eV photon energy is only sufficient to ionise carbon to a C^{2+} state. This 'bleaching' effect allows the EUV laser to ablate a significant amount of material in a single pulse, resulting in high aspect ratio drilling. Plasma refractive index effects are found to be negligible for 26.4eV photons in parylene-N for irradiances below 10^{10}W cm^{-2}. Above this irradiance, focussing and de-focussing effects occur in different regions of the plasma which in part contributes to the enlarging of the surface feature size. The additional heating due to the higher irradiance results in the dominant ionization stage in the plasma being C^{4+} or higher and thus the free electron density becomes comparable to the critical density of the EUV laser and further reduces the efficacy of the laser energy deposition. At lower irradiance, the dominant ionisation stage is lower, the free electron density remains sub-critical and the real component of the dielectric function remains greater than zero.

Over 85% of the ablation is seen to occur within the first half of the laser pulse for the parameters shown in figure 4, and as lateral heat transport dominates at later times, shortening the pulse length would inhibit the enlarging of the feature size by reducing the damaging thermal effects. Alternatively, multiple low fluence pulses could be used to inhibit lateral heat transport, reducing the surface feature size and enabling high aspect ratio, sub-micron sized ablation. To enable multi-pulse simulation, a post-processor has been developed to configure the output of a single pulse simulation. The post-processor analyses output after the end of the first laser pulse, 'removing' any plasma with a temperature greater than the melting point of parylene-N, i.e. resetting the temperature to room (0.025eV) and the density to that of the vacuum ($10^{-7} \times \rho_{solid}$). The simulation is then restarted for a second pulse interacting with the existing ablation crater. Figure 5 indicates how a multiple pulse technique can be utilised to ablate with high uniformity (approximately constant width over ablated depth) and improved surface feature size. Figures 5(a) and 5(b) show the ablation profiles after 1 and 4 pulses respectively, with a focal spot diameter (FWHM) of 500nm and an irradiance of 5×10^9 W cm^{-2}. After 4 pulses, a depth of 4.2 μm has been ablated with a lateral hole size of 1.3μm (FWHM). This hole size will reduce further as the diffraction limit is approached, as shown in figures 5(c) and 5(d). Figures 5(c) and 5(d) show the ablation profiles for a beam of the same irradiance with a focal spot diameter of 200nm after 1 and 2 pulses respectively. An ablated depth of 2.4μm is observed after 2 pulses, with a lateral hole size of 644nm (FWHM). This indicates the potential of this technology for sub-micron size hole drilling under optimised focussing conditions. Using the computational environment described above, the ablative characteristics can be readily optimised depending upon the requirements of the application.

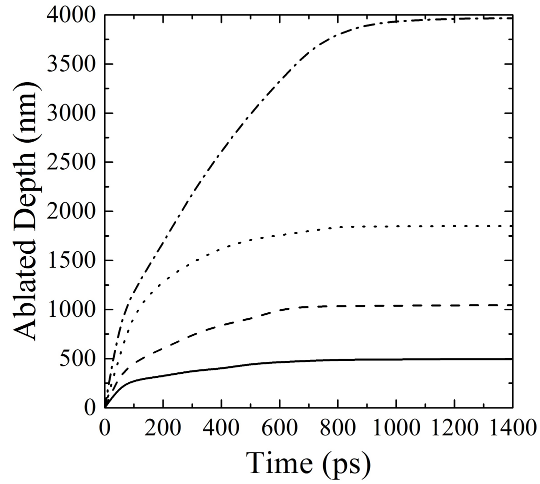

Figure 4. Simulated ablated depth per pulse as a function of time and irradiance for 1×10^{9} W cm^{-2} (solid), 1×10^{10} W cm^{-2} (dashed), 1×10^{11} W cm^{-2} (dotted) and 1×10^{12} W cm^{-2} (dash-dot). The pulse length is 1200ps and the focal spot diameter is 500nm.

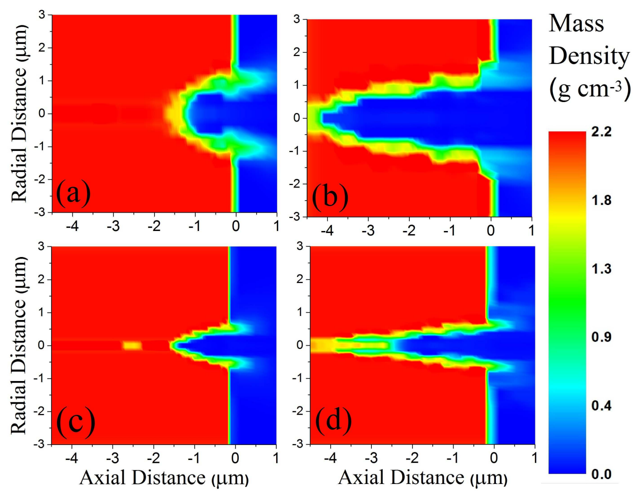

Figure 5. (Color online) Simulated ablation profiles at $t = 1300$ps with an irradiance of 5×10^{9} W cm^{-2} for focal spot diameters of 500nm after (a) 1 pulse and (b) 4 pulses, and 200nm after (c) 1 pulse and (d) 2 pulses.

V. CONCLUSION

This work has demonstrated how a fluid code combined with relevant atomic physics has been used to simulate the heating and subsequent ablation induced by a capillary discharge laser with a photon energy of 26.4 eV. Good agreement is observed between the ablated depth measured experimentally and the predicted depth obtained via simulation for on target irradiances of up to 6×10^9 W cm^{-2}. Increasing the irradiance in the simulation to 1×10^{12} W cm^{-2} has shown an increase in surface feature size due to lateral heat transport. Over 85% of the ablation occurs within the first half of the 1200ps laser pulse and lateral heat transport increases at later time increasing the surface feature size further. Multiple, lower fluence pulses under optimised focussing conditions will be advantageous for applications requiring high-aspect ratio, mesoscale (100nm - 1μm) features and a high level of control over the ablation profile.

ACKNOWLEDGMENTS

This work has been funded by EPSRC grant EP/J019402/1. JJR acknowledges the support of NSF Award PHY1004295.

REFERENCES

[1]G. J. Tallents, "The physics of soft x-ray lasers pumped by electron collisions in laser plasmas," Journal of Physics D: Applied Physics **36**, R259–R276 (2003).

[2]B. W. J. McNeil and N. R. Thompson, "X-ray free-electron lasers," Nature Photonics **4**, 814–821 (2010).

[3]J. J. Rocca, E. C. Hammarsten, E. Jankowska, J. Filevich, M. C. Marconi, S. Moon, and V. N. Shlyaptsev, "Application of extremely compact capillary discharge soft x-ray lasers to dense plasma diagnostics," Physics of Plasmas **10**, 2031 (2003).

[4]B. Benware, C. Macchietto, C. Moreno, and J. J. Rocca, "Demonstration of a High Average Power Tabletop Soft X-Ray Laser," Physical Review Letters **81**, 5804–5807 (1998).

[5]S. Heinbuch, M. Grisham, D. Martz, and J. J. Rocca, "Demonstration of a desk-top size high repetition rate soft x-ray laser," Optics Express **13**, 4050 (2005).

[6]C. D. Macchietto, B. R. Benware, and J. J. Rocca, "Generation of millijoule-level soft-x-ray laser pulses at a 4-Hz repetition rate in a highly saturated tabletop capillary discharge amplifier," Optics Letters **24**, 1115 (1999).

[7]B. A. Reagan, W. Li, L. Urbanski, K. A. Wernsing, C. Salsbury, C. Baumgarten, M. C. Marconi, C. S. Menoni, and J. J. Rocca, "Hour-long continuous operation of a tabletop

soft x-ray laser at 50-100 Hz repetition rate." Optics express **21**, 28380–6 (2013).

[8]M. Berrill, F. Brizuela, B. Langdon, H. Bravo, C. S. Menoni, and J. J. Rocca, "Warm photoionized plasmas created by soft-x-ray laser irradiation of solid targets," Journal of the Optical Society of America B **25**, B32 (2008).

[9]H. Bravo, B. T. Szapiro, P. W. Wachulak, M. C. Marconi, W. Chao, E. H. Anderson, C. S. Menoni, and J. J. Rocca, "Demonstration of Nanomachining With Focused Extreme Ultraviolet Laser Beams," IEEE Journal of Selected Topics in Quantum Electronics **18**, 443–448 (2012).

[10]J.-W. Shin, F. Dong, M. E. Grisham, J. J. Rocca, and E. R. Bernstein, "Extreme ultraviolet photoionization of aldoses and ketoses," Chemical Physics Letters **506**, 161–166 (2011).

[11]K. Tiedtke, A. Azima, N. von Bargen, L. Bittner, S. Bonfigt, S. Düsterer, B. Faatz, U. Frühling, M. Gensch, C. Gerth, N. Guerassimova, U. Hahn, T. Hans, M. Hesse, K. Honkavaar, U. Jastrow, P. Juranic, S. Kapitzki, B. Keitel, T. Kracht, M. Kuhlmann, W. B. Li, M. Martins, T. Núñez, E. Plönjes, H. Redlin, E. L. Saldin, E. A. Schneidmiller, J. R. Schneider, S. Schreiber, N. Stojanovic, F. Tavella, S. Toleikis, R. Treusch, H. Weigelt, M. Wellhöfer, H. Wabnitz, M. V. Yurkov, and J. Feldhaus, "The soft x-ray free-electron laser FLASH at DESY: beamlines, diagnostics and end-stations," New Journal of Physics **11**, 023029 (2009).

[12]J. J. Rocca, V. Shlyaptsev, F. Tomasel, O. Cortázar, D. Hartshorn, and J. Chilla, "Demonstration of a Discharge Pumped Table-Top Soft-X-Ray Laser," Physical Review Letters **73**, 2192–2195 (1994).

[13]J. J. Rocca, F. G. Tomasel, M. C. Marconi, V. N. Shlyaptsev, J. L. A. Chilla, B. T. Szapiro, and G. Giudice, "Discharge-pumped soft-x-ray laser in neon-like argon," Physics of Plasmas **2**, 2547 (1995).

[14]G. J. Pert, "Two-dimensional hydrodynamic models of laser-produced plasmas," Journal of Plasma Physics **41**, 263–280.

[15]G. J. Pert, "Quasi-Lagrangian rezoning of fluid codes maintaining an orthogonal mesh," Journal of Computational Physics **49**, 1–43 (1983).

[16]A. K. Rossall, V. Aslanyan, and G. J. Tallents, "High energy density plasmas produced by x-ray and extreme ultraviolet lasers," in *SPIE Optical Engineering + Applications*, edited by A. Klisnick and C. S. Menoni (International Society for Optics and Photonics, 2013)

pp. 884912–884912–9.

[17]J. Boris and D. Book, "Flux-corrected transport. III. Minimal-error FCT algorithms," Journal of Computational Physics **20**, 397–431 (1976).

[18]R. Courant, E. Isaacson, and M. Rees, "On the solution of nonlinear hyperbolic differential equations by finite differences," Communications on Pure and Applied Mathematics **5**, 243–255 (1952).

[19]L. Spitzer and R. Härm, "Transport Phenomena in a Completely Ionized Gas," Physical Review **89**, 977–981 (1953).

[20]O. Peyrusse, "Coupling of detailed configuration kinetics and hydrodynamics in materials submitted to x-ray free-electron-laser irradiation," Physical Review E **86**, 036403 (2012).

[21]S. L. Thompson, "Improvements in the CHART D radiation-hydrodynamic code I: Analytical equation of state," Sandia National Laboratories Report **SC-RR-70-2** (1970).

[22]S. B. Hansen, J. Bauche, and C. Bauche-Arnoult, "Superconfiguration widths and their effects on atomic models," High Energy Density Physics **7**, 27–37 (2011).

[23]M. F. Gu, "The flexible atomic code," Canadian Journal of Physics **86**, 675–689 (2008).

[24]T. R. Preston, S. M. Vinko, O. Ciricosta, H.-K. Chung, R. W. Lee, and J. S. Wark, "The effects of ionization potential depression on the spectra emitted by hot dense aluminium plasmas," High Energy Density Physics **9**, 258–263 (2013).

[25]V. Aslanyan and G. J. Tallents, "Local thermodynamic equilibrium in rapidly heated high energy density plasmas," Physics of Plasmas **21**, 062702 (2014).

[26]A. K. Rossall and G. J. Tallents, "Generation of Warm Dense Matter using an Argon based Capillary Discharge Laser," High Energy Density Physics (2015), Accepted, In press. DOI:10.1016/j.hedp.2015.04.004.

[27]R. Courant, K. Friedrichs, and H. Lewy, "On the Partial Difference Equations of Mathematical Physics," IBM Journal of Research and Development **11**, 215–234 (1967).